Catalysis

# Mono- and Bimetallic Ni–Co Catalysts in Dry Reforming of Methane

Xuliang Zhang,[a] Zuzana Vajglova,[b] Päivi Mäki-Arvela,[b] Markus Peurla,[c] Heikki Palonen,[d] Dmitry Yu. Murzin,*[b] Svetlana A. Tungatarova,[a, e] Tolkyn S. Baizhumanova,[a, e] and Yermek A. Aubakirov[a]

Several bimetallic Ni–Co catalysts supported on θ-$Al_2O_3$ together with 10 wt% Ni and 10 wt% Co on θ-$Al_2O_3$ were prepared via the incipient wetness method, characterized by X-ray diffraction (XRD), nitrogen adsorption, transmission electron microscopy, temperature programmed reduction, temperature programmed $CO_2$ desorption, Fourier Transformed Infrared Spectroscopy (FTIR) with pyridine adsorption-desorption and tested in dry methane reforming at 700 °C in a fixed bed reactor. According to XRD the metal oxide crystallite sizes decreased from 20 nm for 10 wt% Co/θ-$Al_2O_3$ to 13 nm for 5 wt% Ni-5 wt% Co/θ-$Al_2O_3$, which also showed formation of a mixed oxide alloy. The unit cell parameters for spinel in the fresh catalyst and fcc metal formed during the reaction followed the Vegard's rule. Although monometallic 10 wt% Co/θ-$Al_2O_3$ exhibited high hydrogen consumption, desorption temperature was also high resulting in a rather low activity of 10 wt% Co/θ-$Al_2O_3$ in comparison to bimetallic 5 wt% Ni-5 wt% Co/θ-$Al_2O_3$. The latter exhibited the highest initial activity for hydrogen formation due to its relatively small metal particle size. This catalyst suffered, however, from extensive coking. The most stable catalyst was 10 wt% Ni/θ-$Al_2O_3$ for which the hydrogen yield decreased form 56% to 45% during 100 h time-on-stream. For this catalyst no sintering occurred, opposite to 10 wt% Co/θ-$Al_2O_3$.

## Introduction

Inexpensive supported transition metal catalysts, especially nickel and cobalt catalysts on alumina and silica are very attractive in several industrially important reactions in the presence of hydrogen, such as hydrogenation,[1] hydrodeoxygenation[2,3] and dry methane reforming generated by hydrogen.[4–7] The industrial catalysts should be active, selective and stable. Typically, high metal dispersion is beneficial in several reactions and metal dispersion can be increased, for example, via applying the atomic layer deposition method.[8,9] In addition catalyst stability can be enhanced when metal particles are confined in the support.[10] and specific support properties, such as acidity[2,3] and/or basicity[6] are required. Especially for high temperature reactions, e.g. hydrodeoxygenation[1,2] and dry methane reforming[6,11] high catalyst stability is a necessity. For that purpose also bimetallic Ni–Co catalysts,[12] and Ni–Co alloys have been prepared, which have been reported to be very active, selective and stable in dry methane reforming.[6,13]

In order to understand which kind of properties are required for a stable catalyst for example in dry methane reforming, catalyst characterization and elucidation of the effect of metal dispersion, metal phase composition, acidity, reducibility of metal and changes of the metal faces during the reaction are important. In this work Ni–Co catalysts supported on θ-$Al_2O_3$ with varying Ni and Co content were tested in methane reforming in a continuous fixed bed reactor. Several reports exist in the literature on methane reforming over Ni/γ-$Al_2O_3$.[4–6,14–17] According to our knowledge θ-$Al_2O_3$ has not been previously used as a catalyst support for dry reforming of methane. Although θ-$Al_2O_3$ has typically a lower specific surface area in comparison with γ-$Al_2O_3$, it facilitates higher Ni reducibility.[18] Performance and stability of mono- and bimetallic Ni and Co supported on θ-$Al_2O_3$ with the total metal content of 10 wt% were studied in this work and for the best

[a] X. Zhang, Dr. S. A. Tungatarova, Dr. T. S. Baizhumanova, Prof. Y. A. Aubakirov
Al-Farabi Kazakh National University,
71 al-Farabi ave., Almaty, 050040, Kazakhstan
[b] Dr. Z. Vajglova, Dr. P. Mäki-Arvela, Prof. D. Y. Murzin
Johan Gadolin Process Chemistry Centre,
Åbo Akademi University,
Turku/Åbo, 20500 Finland
E-mail: dmurzin@abo.fi
[c] M. Peurla
Laboratory of Electron Microscopy,
University of Turku,
Turku, 20014, Finland
[d] H. Palonen
Wihuri Physical Laboratory,
Department of Physics and Astronomy,
University of Turku,
20500 Turku, Finland
[e] Dr. S. A. Tungatarova, Dr. T. S. Baizhumanova
D.V. Sokolsky Institute of Fuel,
Catalysis and Electrochemistry,
142 Kunaev str., Almaty, 050010, Kazakhstan

Supporting information for this article is available on the WWW under https://doi.org/10.1002/slct.202100686

catalyst also a stability test for more than one hundred hours time-on-stream was performed. The aim was to correlate the catalysts performance with their properties and elucidate the role of different Ni/Co ratios. Several physico-chemical methods including hydrogen TPR, nitrogen physisorption, XRD, transmission electron microscopy, evolution of the carbon content with CHNS analysis, pyridine adsorption-desorption with FTIR and temperature programmed oxidation of the spent catalysts were used. In addition, catalyst stability was also investigated during methane reforming to carbon oxide and hydrogen.

## Results and discussion

### Characterization of catalysts

Diffractograms of the fresh catalysts 10Ni/θ-$Al_2O_3$, and 5Ni-5Co/θ-$Al_2O_3$ are shown in Figure, while diffractorgram of 9Ni-1Co/θ-$Al_2O_3$, is shown in Figure S1e. The main phase in all catalysts is the θ phase of alumina.[19] In the catalysts with predominant Ni content, a small fraction of α-$Al_2O_3$ was seen,[20] which was even further increased in the spent catalyst. In addition, graphite[21] was found in the spent catalysts containing 5–10 wt% Ni.

The XRD peaks in $Co_3O_4$ spinel are overlapping with those of θ-$Al_2O_3$,[19,22] except at ca. 20° for $Co_3O_4$ which can be better separated from θ-$Al_2O_3$ (Figure 1 and Figure S1). The spinel formation can additionally be confirmed via excluding the presence of CoO, i.e. absence of a peak at 19° for CoO structure[23] and at 37° with CoO with NaCl structure.[24] Furthermore, absence of $CoO_2$ structure of $CoO_2$ was confirmed as a peak at 9° was not present.[25] In addition, XRD pattern for $NiAl_2O_4$ is close to that of $Co_3O_4$.[22,27] It is, however, possible to exclude the presence of $NiAl_2O_4$, since its unit cell parameter is 8.046 Å, while in the current case the measured value is 8.144 Å. Thus is it proposed that $Ni_2Co_2O_4$ can be formed. [27] The amounts of Co and Ni in the spinel calculated based on Table S1 exceeded their nominal loading. It should, however, be stated that the peak at ca. 20° can be assigned also to other structures, such as ($Co_{0.87}Al_{0.13}$) (($Al_{0.60}Co_{0.40}$)$_2O_4$). [28] In that case, the corrected amounts of Co and Ni are consistent with their nominal loading. In the fresh catalysts, Co and Ni are present in the form of $Co_3O_4$, NiO[24] and as $Co_{3-x}Ni_xO_4$ and $Ni_{1-x}Co_xO$, while in the spent catalyst also fcc metal phase was present (Table S1).[29–30] The substitution of Co into NiO is expected to be minimal because the formation of the spinel structure is favored over the formation of NiO across a broad composition range. The spinel structure is found in all other samples but not in 9Ni-1Co/θ-$Al_2O_3$ and 10Ni/θ-$Al_2O_3$ since only Ni cannot form a spinel structure and the catalysts rich in Ni the amount of Co is not sufficient to stabilize the spinel structure. Since the XRD peak position for $Co_3O_4$ is shifted according to the Vegards' rule[29,30] when more nickel is added it is likely that cobalt is being substituted by nickel in the spinel structure. Due to

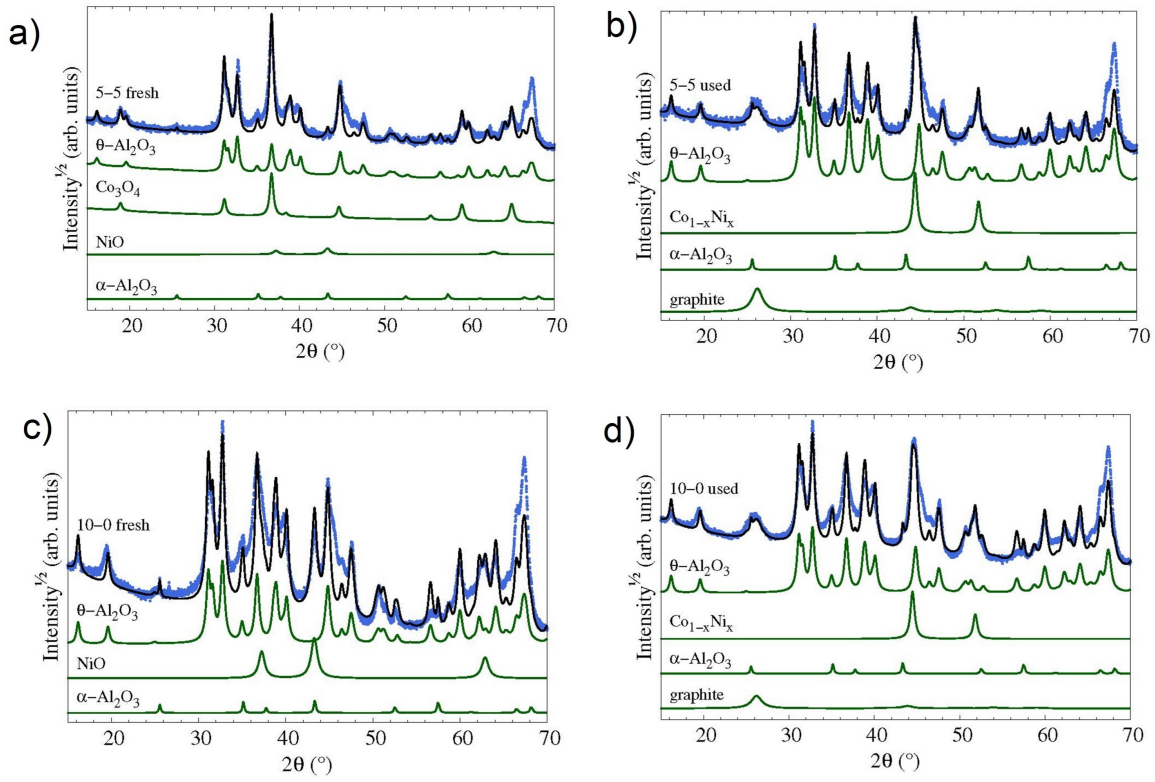


**Figure 1.** XRD patterns of a) fresh and b) spent 5Ni-5Co/θ-$Al_2O_3$, c) fresh and d) spent 10Ni/θ-$Al_2O_3$. The black line shows the Rietveld refinement of the data. The y-axis values are square roots of the intensities.

coexistence of $Co^{2+}$ and $Co^{3+}$ the spinel structure formation is preferred for cobalt oxide.

The unit cell sizes of θ-$Al_2O_3$ and α-$Al_2O_3$ phases agree with the corresponding literature values.[19,20, 22] Both the unit cells of the spinel and metallic fcc structures follow the Vegard's law as can be seen in Figures 2 a and b as also reported in.[27,28] Addition of Ni into $Co_3O_4$ the spinel or alternatively Co into fcc Ni expands the structure as in.[28] When comparing the fresh and the spent catalysts, it can be seen that Co- and Ni-oxides are reduced to the fcc $Co_{1-x}Ni_x$ solid solution (Table S1). Interestingly Co is also in fcc phase,[31] although it should be in the hexagonal phase.

The crystal sizes of the particles were determined from the individual peak widths using the Scherrer formula. The chosen peaks were (202/002), (200), (440), (200) and (002) for θ-$Al_2O_3$, $Ni_{1-x}Co_xO$, $Co_{3-x}Ni_xO_4$, fcc-$Co_{1-x}Ni_x$ and graphite, respectively. Large crystal particle sizes of the spinel structure were observed in the fresh 10Co/θ-$Al_2O_3$, 9Ni-1Co/θ-$Al_2O_3$ and 10Ni/θ-$Al_2O_3$ (Table 1). The fcc metal particle size in the spent catalysts decreased with increasing nickel content most probably due to easier reduction of nickel in comparison to cobalt. [32] Furthermore, the smallest $Co_{3-x}Ni_xO_4$ particles were found in 5Ni-5Co/θ-$Al_2O_3$ which exhibited the same amount of α-$Al_2O_3$ as 10Co/θ-$Al_2O_3$ (Table 1) On the other hand, for 10Ni/θ-$Al_2O_3$ with a higher amount of α-$Al_2O_3$ about the same metal oxide particle size was found as for 10Co/θ-$Al_2O_3$ indicating that the amount of α-$Al_2O_3$ did not have any major effect on metal oxide particle size. The spent catalysts exhibiting the nickel content between 5–10 wt% contained additionally crystalline graphite with the size of 4–6 nm. The crystal sizes of θ-$Al_2O_3$ were the same for different catalysts decreasing slightly for the spent catalysts. The α-$Al_2O_3$ phase has much large crystal sizes, at least ca. 50 nm.

The specific surface area, pore volume and micropore area for the fresh and spent Ni/θ-$Al_2O_3$, Co/θ-$Al_2O_3$ and Ni–Co/θ-$Al_2O_3$ catalysts are given in Figures S2 and S3 and in Table 2. The catalysts exhibited only the mesopores. Slightly increased surface and micropore areas were determined for the spent 10Co/θ-$Al_2O_3$ and 1Ni-9Co/θ-$Al_2O_3$ catalysts (Figure S3a), while the surface area of the fresh and spent 10Ni/θ-$Al_2O_3$ remained the same. Furthermore, for the spent 5Ni-5Co/θ-$Al_2O_3$ a minor increase of the specific surface area was observed in comparison to the fresh one. These results indicate that coking of catalysts occurs mainly at the outer surface, since more carbon was formed over nickel containing catalysts in comparison to Co-catalyst (Table 3). The pore size distribution of the spent catalysts shows a shift from larger pores to smaller ones compared to the fresh ones (Figure S2). This indicates the clogging of the larger pores during the reaction. The specific surface area of 10 wt% Ni/θ-$Al_2O_3$ reported in[18] correlates quite well with the current data. Typically surface area for θ-$Al_2O_3$ is also lower than that for γ-$Al_2O_3$.[18]

TEM images of fresh and spent mono-and bimetallic catalysts (Figures 4 and S4) and the corresponding average

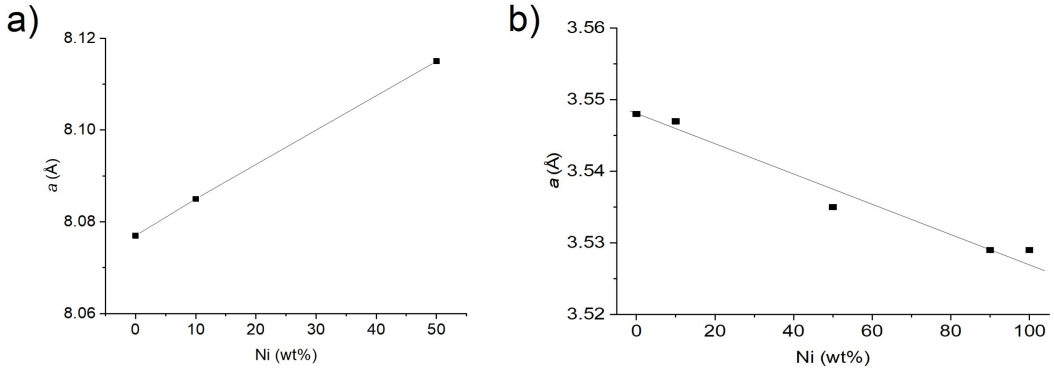


**Figure 2.** The unit cell parameters for a) the spinel $Co_{3-x}Ni_xO_4$ in which 100 wt% Ni equals to $x = 3$ (observe no spinel was present in 9Ni-1Co/θ-$Al_2O_3$ and 10Ni/θ-$Al_2O_3$) and b) metallic $Co_{1-x}Ni_x$ phase for different spent catalysts (see Table 1). The line corresponds to the Vegard's law.

**Table 1.** Results from TEM. In parenthesis data for the spent catalysts.

| Catalyst | Crystal size | | | | |
|---|---|---|---|---|---|
| | $D_{\theta\text{-}Al2O3}$ (nm) | $D_{Co3-xNixO4}$ (nm) | $D_{Ni1-xCoxO}$ (nm) | $D_{Co1-xNix}$ (nm) | $D_{TEM}$ (nm) |
| 10Co/θ-$Al_2O_3$ | 24 (21) | 18 | n.d. | (20) | 14 (17) |
| 1Ni-9Co/θ-$Al_2O_3$ | 23 (22) | 16 | n.d. | (18) | 39 (28) |
| 3Ni-7Co/θ-$Al_2O_3$ | 23 (21) | 13 (17) | n.d. | n.d. | 19 (25) |
| 5Ni-5Co/θ-$Al_2O_3$ | 23 (21) | 13 | [a] | (14) | 22 (17) |
| 7Ni-3Co/θ-$Al_2O_3$ | 23 (23) | [a] | [a] (13) | n.d. | 17 (29) |
| 9Ni-1Co/θ-$Al_2O_3$ | 23 (23) | [a] | 17 | (13) | 21 (17) |
| 10Ni/θ-$Al_2O_3$ | 23 (23) | [a] | 16 | (12) | 17 (16) |

[a] below the detection limit.

**Table 2.** Textural properties of Ni–Co/θ-$Al_2O_3$ catalysts.

| Catalyst | A* $m^2/g$ | $V_p$** $cm^3/g$ | $d_p$ nm | $A_{ex}$*** $m^2/g$ | $A_\mu$*** $m^2/g$ |
|---|---|---|---|---|---|
| 5Ni-5Co/θ-$Al_2O_3$ (P) | 61 | 0.39 | 17.3 | 56 | 5 |
| 10Co/θ-$Al_2O_3$ (F) | 60 | 0.37 | 17.1 | 52 | 7 |
| 1Ni-9Co/θ-$Al_2O_3$ (F) | 61 | 0.37 | 16.9 | 54 | 7 |
| 5Ni-5Co/θ-$Al_2O_3$ (F) | 57 | 0.35 | 16.0 | 52 | 6 |
| 9Ni-1Co/θ-$Al_2O_3$ (F) | 65 | 0.38 | 16.5 | 59 | 6 |
| 10Ni/θ-$Al_2O_3$ (F) | 64 | 0.37 | 16.2 | 59 | 6 |
| 10 wt% Ni/θ-$Al_2O_3$[18] | 76 | 0.26 | 14.0 | – | – |
| 10Co/θ-$Al_2O_3$ (S) | 74 | 0.33 | 16.5 | 61 | 14 |
| 1Ni-9Co/θ-$Al_2O_3$ (S) | 72 | 0.33 | 16.5 | 58 | 13 |
| 5Ni-5Co/θ-$Al_2O_3$ (S) | 63 | 0.33 | 16.2 | 57 | 6 |
| 9Ni-1Co/θ-$Al_2O_3$ (S) | 64 | 0.32 | 16.1 | 57 | 7 |
| 10Ni/θ-$Al_2O_3$ (S) | 65 | 0.36 | 16.2 | 57 | 8 |

P – fresh powder form, F – fresh catalyst, S – spent catalyst, A – specific surface area (BET method), $V_p$ – specific pore volume, $d_p$ – median pore diameter (BJH desorption method), $A_{ex}$ – external surface area, $A_\mu$ – micropore area. *determined by BET method, ** determined by BJH method, *** determined by t-plot method.

metal (oxide) particle sizes are shown in Table 1 and in Figure S5. Furthermore, uneven distribution of different elements can be observed (Figures 4 and S4). For monometallic 10Ni/θ-$Al_2O_3$ the metal particle size decreased during the reaction, being in accordance with XRD results (Figure 3, Table 1). On the other hand, the particle size for 10 Co/θ-$Al_2O_3$ increased from fresh to spent one as also confirmed by XRD (Table 1). It can be seen from the particle size distribution (Figure S5) determined from TEM images (Figures 4 and S4) and from the average particle size (Table 1) that in most cases metal oxide particles were smaller in the spent catalysts. These results correlate well with the XRD results.

From SEM images of the fresh and spent 10Ni/θ-$Al_2O_3$ and 5Ni-5Co/θ-$Al_2O_3$ (Figure S6) it can be seen that especially in the mapping image of the spent 5Ni-5Co/θ-$Al_2O_3$ catalyst that the metal on the catalyst surface is slightly covered by carbon after the reaction. The Ni and Co mapping images (Figure S7) in 5Ni-5Co//θ-$Al_2O_3$ catalysts show that these elements remain in the same position also after the reaction. Figure S7 also illustrates that Ni and Co are concentrated in different places non-uniformly across the surface.

The results from acidity measurements with FTIR pyridine adsorption-desorption for three different catalysts (Table S2) show that the highest acidity was determined for 5Ni-5Co/θ-$Al_2O_3$ and the lowest for 10Co/θ-$Al_2O_3$.

According to the temperature programmed reduction an increase in the Co content resulted in a higher reduction temperature (Table 3, Figure 5). The lowest hydrogen consumption was obtained in hydrogen TPR (Table 3) for the monometallic 10Ni/θ-$Al_2O_3$. Interactions between NiO and $Al_2O_3$ are relatively strong requiring a higher temperature for nickel oxide reduction compared to the bulk oxide. [18] In general, nickel-based catalysts have a lower reduction temperature because Ni is much easier to be reduced than Co. [32] When Ni content decreased, the peak area for hydrogen consumption gradually increased (Table 3). The 10Co/θ-$Al_2O_3$ catalyst has the highest reduction temperature and the largest degree of reduction, although its crystal particle size is larger than for 5Ni-5Co/θ-$Al_2O_3$. According to the literature[33] 1 wt% Co-10 wt% Ni supported on γ-$Al_2O_3$ exhibited a peak at 560 °C assigned to NiO reduction. It should, however, be stated that the reducibility of Ni supported on θ-$Al_2O_3$ is better than on γ-$Al_2O_3$ with the peak maxima for hydrogen consumption for 10 wt% Ni/θ-$Al_2O_3$ at 380 °C and 490 °C. [34] In the current case the main hydrogen consumption peaks for 10Ni/θ-$Al_2O_3$ were found at 450 °C and 580–610 °C, with the latter being close to the literature. [34] It should, however, be stated here that the first reduction peak of 10Ni/θ-$Al_2O_3$, related to reduction of the bulk nickel oxide, [34] is rather small indicating that NiO is not easily reduced or its amount is low. In addition, the main hydrogen consumption peak for 10Ni/θ-$Al_2O_3$ was found previously[18] to be close to 600 °C which corresponds very well to the current case.

The relative area of hydrogen consumed is the smallest for 9Ni-1Co/θ-$Al_2O_3$ among the bimetallic catalysts and even lower for 10Ni/θ-$Al_2O_3$ indicating that it is difficult to reduce NiO particles. Introduction of Co makes reduction of NiO easier with an increase of Co content and for Co–Ni/$Al_2O_3$ catalyst a peak at 345 °C became visible in TPR.[33] The interpretation of the current TPR results is not straightforward because the TPR profiles are rather complex and the literature on Ni supported on θ-$Al_2O_3$ is very scarce. [18,34] Furthermore, it is known that the peak position in TPR can be determined by 1) metal loading, 2) support nature, 3) presence of the second metal and 4) the size of metal particles. [33,35]

CHNS results showed that the highest amount of carbon was accumulated on the spent 5Ni-5Co/θ-$Al_2O_3$, while only minor amounts of coke were detected on 1Ni-9Co/θ-$Al_2O_3$ and 10Ni/θ-$Al_2O_3$. Furthermore, no carbon was observed in the spent 10Co/θ-$Al_2O_3$ (Table 3). When comparing these results with the literature[11] it can be concluded that monometallic Ni supported on γ-$Al_2O_3$ accumulated 10 fold more carbon in

**Table 3.** Results from hydrogen TPR and CHNS analysis from the fresh and carbon content in the spent catalysts.

| Entry | Catalyst | Hydrogen TPR | | | Carbon content by CHNS analysis (wt%) |
|---|---|---|---|---|---|
| | | $T_{max1}$ (°C) | $T_{max2}$ (°C) | Area of consumed hydrogen (a.u.) | |
| 1 | 10Co/θ-$Al_2O_3$ | 400 | 680-740 | 26.6 | 0.3 |
| 2 | 1Ni-9Co/θ-$Al_2O_3$ | 360 | 670-700 | 23.6 | 1.2 |
| 3 | 5Ni-5Co/θ-$Al_2O_3$ | 310 | 420, 580–600 | 23.7 | 14.3 |
| 4 | 9Ni-1Co/θ-$Al_2O_3$ | 309 | 400, 640–650 | 17.1 | 4.7 |
| 5 | 10Ni/θ-$Al_2O_3$ | 299 | 450, 580–610 | 12.7 | 3.1 |

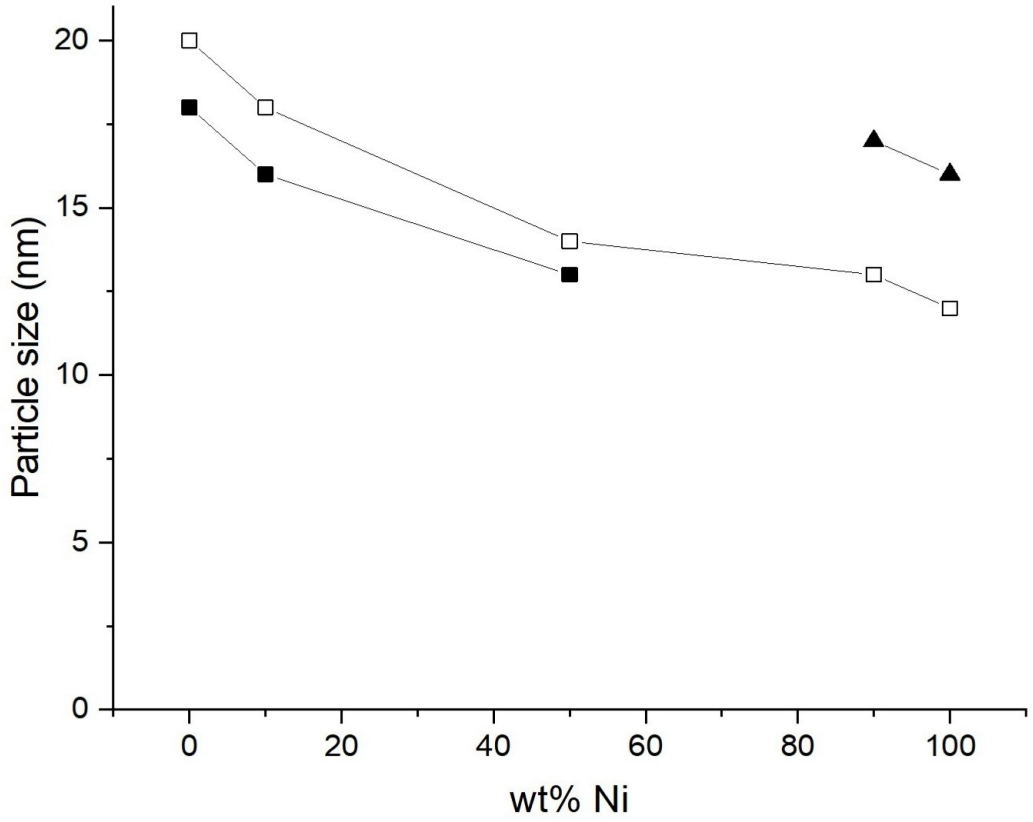


**Figure 3.** The spinel (■) and metal oxide particle size (▲) in the fresh catalysts and metal particle size (□) in the spent catalysts determined by XRD (Table 1) as a function of nickel content in Ni–Co/ θ-$Al_2O_3$ catalysts.

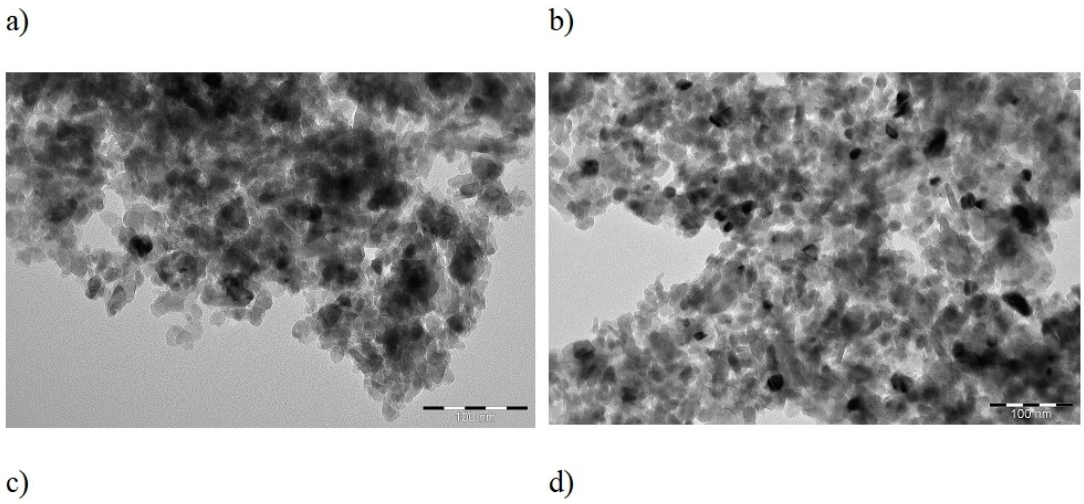


**Figure 4.** TEM images of a) fresh and b) spent 5Ni-5Co/θ-$Al_2O_3$ and c) fresh and d) 10Ni/θ-$Al_2O_3$.

comparison with the corresponding monometallic Co catalyst in dry methane reforming analogously to the current results. The highest carbon content was observed for 5Ni-5Co/θ-$Al_2O_3$, which exhibited the highest methane conversion among all catalysts (see below). Despite a high amount of coke, no carbon filaments were visible, opposite to e.g. carbon nanotubes formed in methane reforming over Co–Mo/$ZrO_2$/$Al_2O_3$. [32]

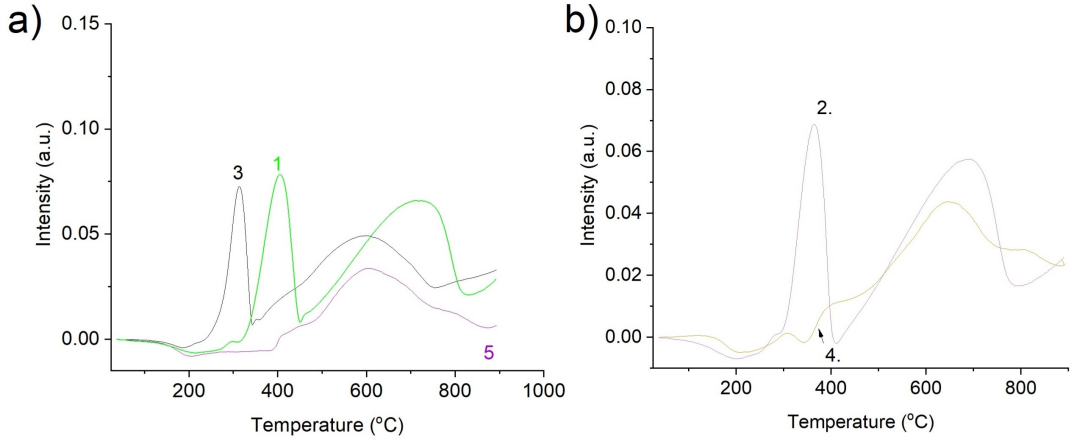


**Figure 5.** a) b) TPR patterns of different catalysts. Notation: 1) 10Co/θ-$Al_2O_3$ 2) 1Ni-9Co/θ-$Al_2O_3$, 3) 5Ni-5Co/θ-$Al_2O_3$ f, 4) 9Ni-1Co/θ-$Al_2O_3$ and 5) 10Ni/θ-$Al_2O_3$.

### Catalytic results

The performance of monometallic Ni and Co supported on θ-$Al_2O_3$ as well as their bimetallic counterparts was studied in methane reforming at 700 °C (Table 4). The highest initial conversion of methane was observed for the bimetallic 5Ni-5Co/θ-$Al_2O_3$, which exhibited the smallest metal oxide particles (Table 1, Figure 6a). The higher initial activity of 5Ni-5Co/θ-$Al_2O_3$ can be explained by the presence of relatively small metal oxide particles in the fresh catalyst (Table 1), which are also prone to deactivation. [36] It was reported in[36] that rather small particles (6-10 nm) after being encapsulated in coke are not active in methane reforming. The metal oxide particle size of 10Co/θ-$Al_2O_3$ is also larger than that for 10Ni/θ-$Al_2O_3$, which can explain the better performance of the latter catalyst in comparison to the former one. Ni per se can be more active, because of electronic properties, etc. Methane conversion after 2 h TOS for three studied catalysts could also be correlated with catalyst acidity determined by FTIR pyridine adsorption-desorption (Figure 6c), i.e. methane conversion increased with

**Table 4.** Conversion of methane and $CO_2$ and the degree of deactivation in methane reforming at 700 °C, $CH_4$:$CO_2$:Ar = 1 : 1 : 1 ratio and GHSV = 6000 $h^{-1}$ and comparison with the literature.

| Entry | Catalyst | Methane conversion after 2 h (after 12 h) | $CO_2$ conversion after 2 h (after 12 h) | Deactivation degree based on methane conversion (%)[a] | Deactivation degree based on $CO_2$ conversion (%)[b] |
|---|---|---|---|---|---|
| 1 | 10Co/θ-$Al_2O_3$ | 64 (65) | 69 (50) | 0 | 28.8 |
| 2 | 1Ni-9Co/θ-$Al_2O_3$ | 65 (55) | 72 (59) | 17.8 | 18.6 |
| 3 | 5Ni-5Co/θ-$Al_2O_3$ | 75 (49) | 82 (59) | 34.2 | 28.5 |
| 4 | 9Ni-1Co/θ-$Al_2O_3$ | 58 (46) | 65.5 (57) | 15 | 13.7 |
| 5 | 10Ni/θ-$Al_2O_3$ | 72 (66) | 76.3 (73) | 9 | 4 |
| 6 | 9 wt% Co/γ-$Al_2O_3$[16] | 72[c] | n.d. | 1 | n.d |
| 7 | 9 wt% Co/γ-$Al_2O_3$[36] | 75[d] | 83[d] | 0 | n.d. |
| 8 | 9 wt% Ni/γ-$Al_2O_3$[4] | 54[c] | n.d. | 10 | n.d. |
| 9 | 5 wt% Ni/γ-$Al_2O_3$[5] | 67[e] (68) | 73.5 (72) | 0 | 2 |
| 10 | 5 wt% Ni- 5 wt Co/γ-$Al_2O_3$[17] | 76[f] | n.d. | 0 | n.d. |
| 11 | 15 wt% Co/γ-$Al_2O_3$[4] | negligible | n.d. | n.d. | n.d. |

[a] Deactivation degree after 12 h TOS was calculated as follows:

$$D_{deact} = \frac{X_{CH4,2h} - X_{CH4,12h}}{X_{CH4,2h}} * 100\%$$

where X is conversion,
[b] deactivation degree based on $CO_2$ conversion was calculated analogously to methane, using instead $CO_2$ conversion after 2 and 12 h time-on-stream,
[c] 700 °C, GHSV = 20 000 $h^{-1}$, after 6 h
[d] 700 °C, 22000 $h^{-1}$, after 6 h
[e] 700 °C
[f] 700 °C, 800 °C, GHSV = 998400 ml $g_{cat}^{-1}$ $h^{-1}$, 60 h time-on-stream

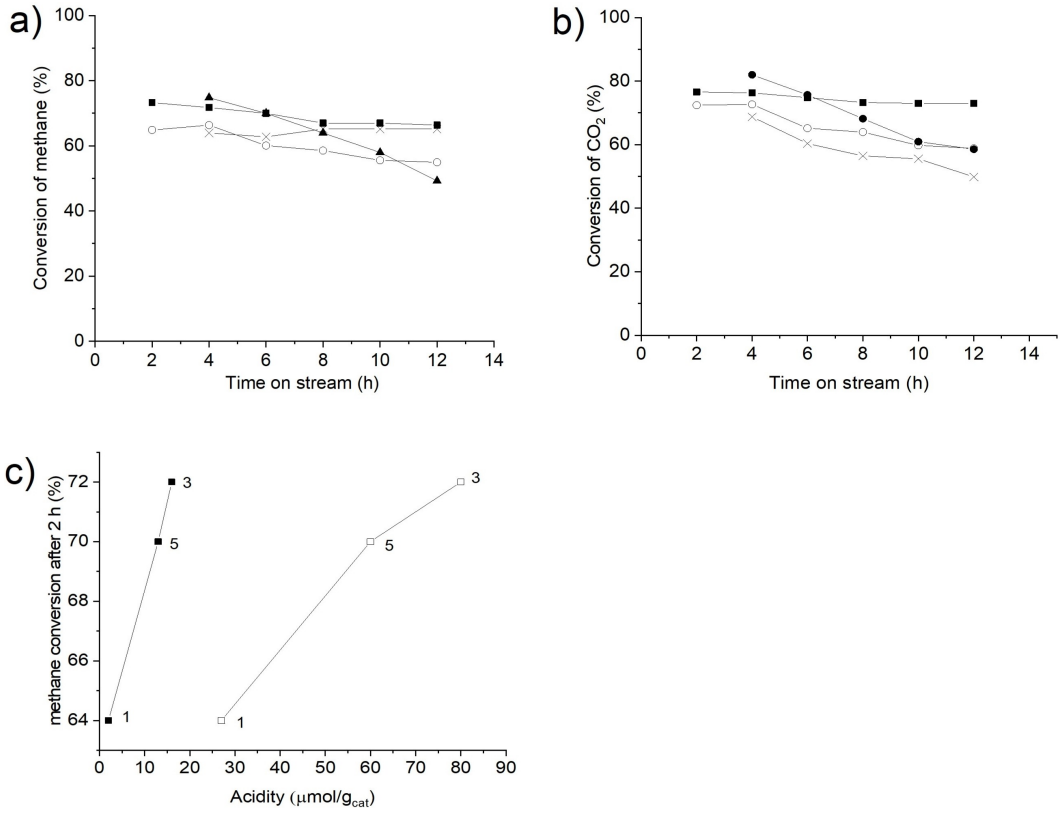


**Figure 6.** a) Methane conversion and b) $CO_2$ conversion as a function of time-on-stream over 1 (x), 2 (o), 3 (▲) and 5 (■) catalysts and c) as a function of Brønsted (■) and Lewis acidity (□) in methane dry reforming for 1) 10Co/θ-$Al_2O_3$, 3) 5Ni-5Co/θ-$Al_2O_3$ and 5) 10Ni/θ-$Al_2O_3$ catalysts. The notation is same as in Table 4.

increasing acidity. Furthermore, deactivation is more prominent with increasing Lewis acidity. This result correlates well with the literature,[37] reporting that higher acidity leads to more coking in dry methane reforming over Ni/$Al_2O_3$ modified with P. On the other hand, methane conversion increased with increasing time on stream for 10Co/θ-$Al_2O_3$ because of catalyst activation during the stability test. 1Ni-9Co/θ-$Al_2O_3$ catalyst exhibited initially nearly the same methane conversion, as 10Co/θ-$Al_2O_3$, however, the former catalyst was deactivated rapidly with increasing time-on-stream (Table 4).

Lower conversion levels of $CH_4$ were obtained after 12 h TOS over 1Ni-9Co/θ-$Al_2O_3$, 5Ni-5Co/θ-$Al_2O_3$, and 9Ni-1Co/θ-$Al_2O_3$ and two latter catalysts contained more than 5 wt% graphite according to XRD (Table S1). The highest methane conversions after prolonged TOS were, however, obtained over monometallic catalysts, 10Ni/θ-$Al_2O_3$ and 10Co/θ-$Al_2O_3$. When comparing the performance of 10Ni/θ-$Al_2O_3$ in the current case with that of 9 wt% Ni/γ-$Al_2O_3$ reported in[16] it can be seen that in this work methane conversion after 12 h TOS is much better than that obtained with 9 wt% Ni/γ-$Al_2O_3$ after 6 h TOS at 700 °C. This might be due to a degree of Ni reduction for Ni/γ-$Al_2O_3$ in comparison to Ni/θ-$Al_2O_3$ because of a lower amount of surface defects present in θ-$Al_2O_3$.[18]

$CO_2$ conversion obtained after 2 h and 12 h time-on-stream remained nearly constant for 10Ni/θ-$Al_2O_3$, while it dropped from 69% to 50% for 10Co/θ-$Al_2O_3$ (Figure 6b). As a comparison with literature the ratios between methane to $CO_2$ conversion after 2 h TOS at 700 °C for 5Ni-5Co/θ-$Al_2O_3$ in the current work and for 5 wt% Ni-5 wt% Co/γ-$Al_2O_3$[14] were very close to each other (0.91 and 0.91,[14] respectively), despite different metal crystallite sizes (13 nm and 7.7 nm, [14] respectively). Only monometallic 10Ni/θ-$Al_2O_3$ was stable in transforming $CO_2$ (Figure 6b). Noteworthy is that the spent 10Ni/θ-$Al_2O_3$ contained also the smallest fcc metal particles determined by XRD after dry methane reforming after 12 h TOS (Table 1), which can partially explain its stable performance. On the other hand, $CO_2$ conversion was not stable over monometallic 10Co/θ-$Al_2O_3$ or bimetallic Ni–Co/θ-$Al_2O_3$ catalysts. It is difficult to compare directly the current results with the literature data, because interactions between the support and the metal are different. When using γ-$Al_2O_3$ as a support, it was demonstrated in[4] that 15 wt% Co/$Al_2O_3$ was not efficient in methane dry reforming contrary to 9 wt% Co/γ-$Al_2O_3$ with Co particles of the size 14.1 nm (Table 4).

The degree of deactivation calculated based on methane conversion was also the highest for 5Ni-5Co/θ-$Al_2O_3$ being the lowest for 10Co/θ-$Al_2O_3$ which also displayed some sintering according to XRD (Figure 7, Table 4). Analysis of catalyst stability in methane conversion for different catalysts based on methane conversion (Table 4), indicates that deactivation was

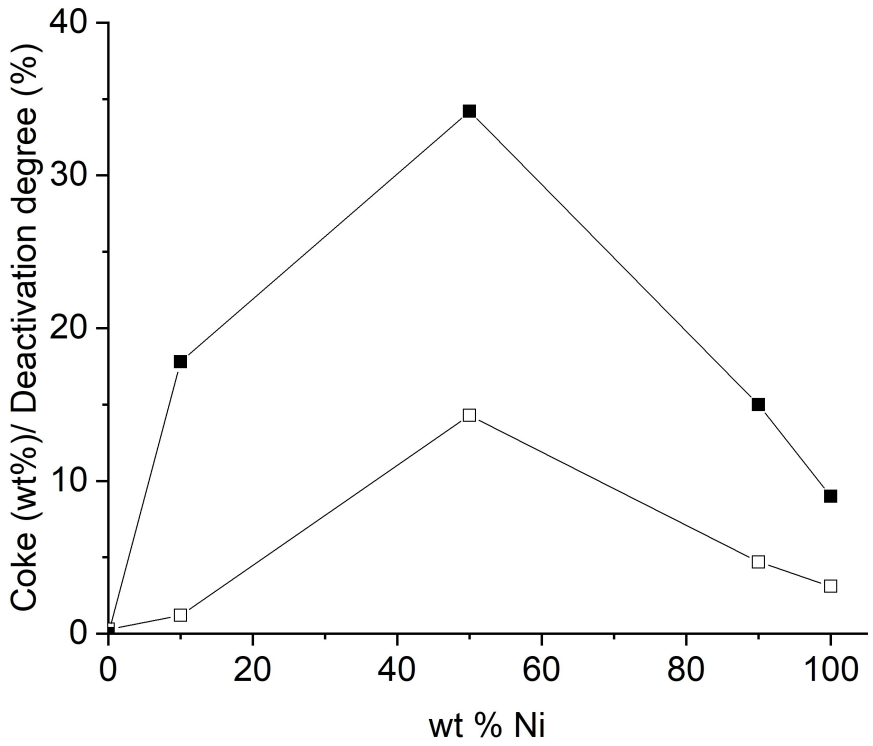


**Figure 7.** Coke formation (□) and deactivation degree calculated from methane conversion after 12 h (■) as a function of Ni content in the catalyst.

the highest for 5Ni-5Co/θ-$Al_2O_3$, which is correlating well with the carbon content in the spent catalysts determined by CHNS (Figure 7). Better results after prolonged time-on-stream were obtained for monometallic Ni/θ-$Al_2O_3$. In the case of Ni containing catalysts, graphite was formed when Ni loading was above 5 wt% (Table S1) concomitant with a partial transformation of the Ni–Co oxide phase to a metallic Co–Ni alloy.

Generally, one of the reasons for catalyst deactivation may be carbon deposition in the catalyst pores.[38,39] Ni–Co catalysts supported on θ-$Al_2O_3$ exhibited large pores (Table 2), which is beneficial for stability. Furthermore, especially methane cracking is one reason for formation coke over Ni/γ-$Al_2O_3$. [6] Coking of bimetallic 5 wt% Ni-10 wt% Co/γ-$Al_2O_3$ was also observed during dry methane reforming at 700 °C. [14] In addition monometallic spent 9 wt% Ni/γ-$Al_2O_3$ used in dry reforming of methane at 700 °C contained coke free metal particles indicating that the catalyst exhibited activity after 6 h TOS.[16] Dehydrogenation of methane to hydrogen and carbon occurs on metal sites, which most probably are rapidly deactivated, especially in the case of Ni. $H_2$/CO ratio was 1 with monometallic Co catalyst (Table 5, entry 1) as well as for 1Ni-9Co/θ-$Al_2O_3$, while for the catalysts containing more Ni, this ratio exceeded unity. Such high $H_2$/CO ratio indicates either methane cracking or the water gas shift reaction.[40] A temperature increase was beneficial for $H_2$/CO ratios giving a value of ca. 1.5 in methane dry reforming at 900 °C. [41] On the other hand, the Fischer-Tropsch process can be successfully performed even at the $H_2$/CO ratios exceeding one. [42]

The highest rate for hydrogen formation was observed for 5Ni-5Co/θ-$Al_2O_3$ after 2 h TOS (Figure 8a). This catalyst exhibited small metal oxide particle size (Table 1) and a relatively high hydrogen consumption in TPR. Furthermore, the low temperature peak in hydrogen TPR was present at 299 °C (Table 3). As can be seen from Figure 8b, the catalyst with the

**Table 5.** Yields of hydrogen, methane and their ratio in methane reforming at 700 °C, $CH_4$:$CO_2$:Ar = 1 : 1 : 1 ratio and GHSV = 6000 $h^{-1}$ and comparison with the literature.

| Entry | Catalyst | Yield of $H_2$ after 12 h (%) | Yield of CO after 12 h (%) | $H_2$/CO after 12 h | Ref. |
|---|---|---|---|---|---|
| 1 | 10Co/θ-$Al_2O_3$ | 24.1 | 24.1 | 1.0 | This work |
| 2 | 1Ni-9Co/θ-$Al_2O_3$ | 25.8 | 25.0 | 1.0 | This work |
| 3 | 5Ni-5Co/θ-$Al_2O_3$ | 29.0 | 22.8 | 1.3 | This work |
| 4 | 9Ni-1Co/θ-$Al_2O_3$ | 28.0 | 22.0 | 1.3 | This work |
| 5 | 10Ni/θ-$Al_2O_3$ | 33.3 | 30.3 | 1.1 | This work |
| 6 | 9 wt% Co/γ-$Al_2O_3$ | n.m. | n.m. | n.m. | [16] |
| 7 | 9 wt% Co/γ-$Al_2O_3$ | n.d. | n.d. | n.d. | [36] |

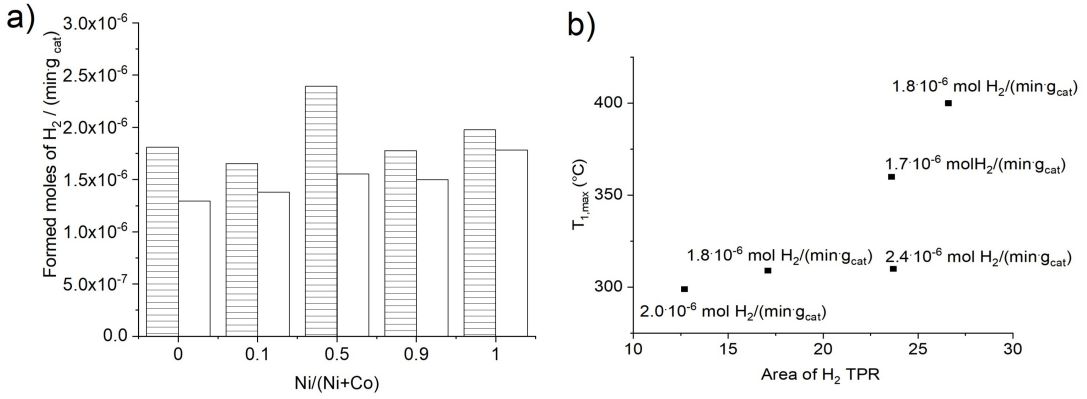


**Figure 8.** a) formation rate of $H_2$ after 2 h (with stripes) and 12 h (empty rectangular) time-on-stream as a function of Ni weight fraction in different catalysts. b) $T_{max,1}$ as a function of the relative total area of $H_2$ TPR for different catalysts. The graph contains also the specific hydrogen formation rates. Conditions: 700 °C, $CH_4$:$CO_2$:Ar = 1 : 1 : 1 ratio and GHSV = 6000 $h^{-1}$.

low $T_{max,\ 1}$ at the same time exhibiting a large peak area of consumed hydrogen was the most active one. On the other hand, if the $T_{max,1}$ was low, as was the case for 10Ni/θ-$Al_2O_3$, its hydrogen formation rate was quite low. Interestingly 10Co/θ-$Al_2O_3$ exhibited high $T_{1,max}$ and a large peak area for hydrogen consumption giving a rather low hydrogen formation rate. This result is in accordance with the work of Cao et al., [6] who proposed that strong interactions between Ni and Co are beneficial for activity enhancement in dry methane reforming.

The highest selectivity to hydrogen after 2 h TOS was obtained over 5Ni-5Co/θ-$Al_2O_3$ while after 12 h TOS 9Co-1Ni/θ-$Al_2O_3$ displayed the highest selectivity (Figure 9). In 5Ni-5Co/θ-$Al_2O_3$ small metallic alloy particles of fcc structure were formed during the reaction probably active in methane decomposition rather than in methane reforming.[40] Hydrogen selectivity decreased substantially to ca. 57% for 10Co/θ-$Al_2O_3$ most probably due to sintering of metal oxide particles (Table 1).

Based on preliminary experiments with all five catalysts, showing the best results for 10Ni/θ-$Al_2O_3$, it was decided to perform stability tests in dry methane reforming with this catalyst.

Over 10Ni/θ-$Al_2O_3$ methane conversion decreased from 73% to 66% between 2 h and 12 h TOS (Figure 10a). Analogously methane conversion decreased only slightly during 65 h time-on-stream[5] in dry methane reforming at 700 °C over 5 wt% Ni/γ-$Al_2O_3$ pre-reduced at the same temperature. It was also pointed out in[4] that when Ni/γ-$Al_2O_3$ is reduced at high temperature, its stability is increased. In the current work activity of 10Ni/θ-$Al_2O_3$ after 100 h TOS decreased slightly, however, hydrogen yield decreased from 56% at 2 h TOS to 51% at 8 h TOS and only to 46% after 100 h TOS. When the catalyst was reduced after 100 h TOS under hydrogen flow, its activity increased and at the same time the hydrogen yield was elevated from 46% to 51% after 100 hours (Figure 10b).

The monometallic 10Ni/θ-$Al_2O_3$ was quite stable and did not show any sintering in the preliminary catalyst screening (Table 1, Table 4). The $H_2$/CO ratio over this catalyst after 18 h was 1.1. Typically, higher $CO_2$ conversion in comparison to methane conversion has been reported over Ni/γ-$Al_2O_3$ catalyst

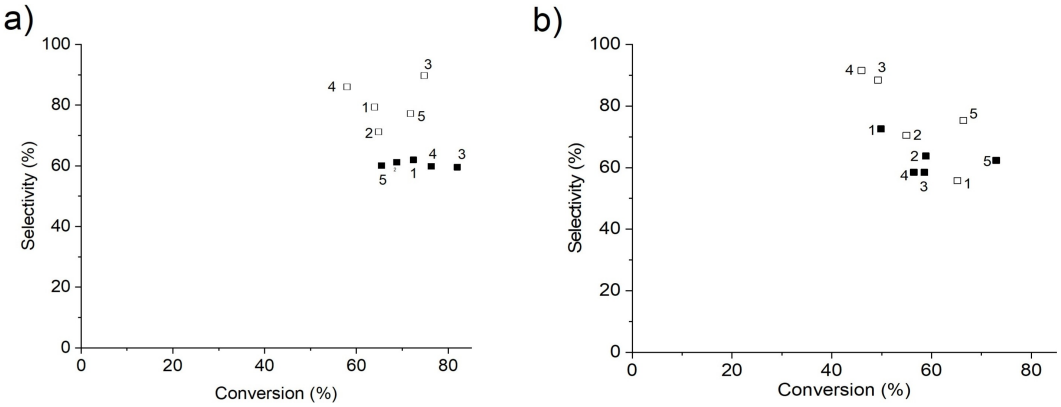


**Figure 9.** Selectivity to $H_2$ and CO calculated as a function of methane and $CO_2$ conversion, respectively over different catalysts after a) 2 h and b) 12 h time-on-stream. Notation: open symbol $H_2$ selectivity, closed symbol CO selectivity, 1) 10Co/θ-$Al_2O_3$ 2) 1Ni-9Co/θ-$Al_2O_3$, 3) 5Ni-5Co/θ-$Al_2O_3$, 4) 9Ni-1Co/θ-$Al_2O_3$ and 5) 10Ni/θ-$Al_2O_3$.

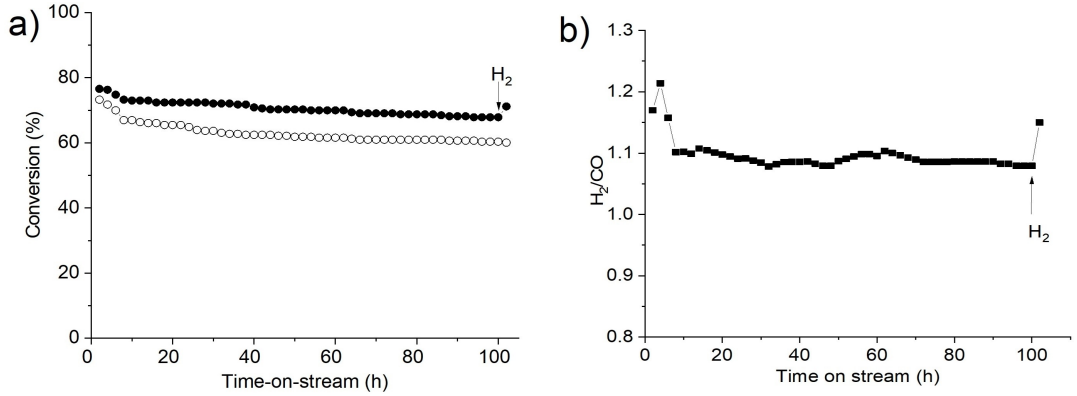


**Figure 10.** Conversion of $CO_2$ and $CH_4$ over 10Ni/θ-$Al_2O_3$ as a function of time-on-stream, hydrogen treatment performed after 100 h TOS and b) the corresponding $H_2$/CO ratio, conditions 700 °C, $CH_4$:$CO_2$:Ar = 1 : 1 : 1 ratio and GHSV = 6000 $h^{-1}$. Notation: $X_{CH4}$ (o) and $X_{CO2}$ (●), where X is conversion.

in dry methane reforming.[14,15] At the same time $H_2$/CO ratio is lower than the one reported earlier. [10] In the current case over Ni supported catalyst conversion of $CO_2$ was higher than methane conversion, while the $H_2$/CO ratio exceeded unity (Figure 10b), indicating that the Boudourd reaction[32]

$$2CO\ (g) \rightleftarrows C(s) + CO_2(g) \quad (1)$$

which could occur instead of the reverse water gas shift reaction. On the other hand $H_2$/CO ratio decreased rapidly with increasing TOS for 10Co/θ-$Al_2O_3$ reaching 0.87 at 38 h TOS.

## Conclusions

Several bimetallic Ni–Co catalysts supported on θ-$Al_2O_3$ with a varying ratio of Ni to Co were synthesized in addition to monometallic Ni and Co catalysts. These materials were characterized by several physico-chemical methods and tested in dry reforming of methane at 700 °C. The transmission electron microscopy results revealed that the smallest metal oxide crystallite sizes were found for monometallic 10 wt% Co/θ-$Al_2O_3$ and 10 wt% Ni/θ-$Al_2O_3$. The formation of Co–Ni-spinel and oxide alloy phases was confirmed in bimetallic catalysts.

The bimetallic 5 wt% Ni-5 wt% Co/θ-$Al_2O_3$ exhibited the highest initial activity for hydrogen formation giving $CH_4$ and $CO_2$ conversion of 75%, and 82%, respectively at 700°C. Its activity, however, declined rapidly with increasing time-on-stream along with a phase transition of the spinel type metal oxide to fcc mixed Co–Ni metal structure. The most stable catalyst was monometallic 10 wt% Ni/θ-$Al_2O_3$ for which still the hydrogen yield decreased form 56% to 45% during 100 h TOS while concomitant with a change of the mixed Co–Ni oxide to fcc type metallic alloy.

## Supporting Information Summary

Supporting Information contains the experimental section, data on adsorption isotherms, specific surface area, particle size distribution based on TEM, SEM images, metal mapping, and acidity.

## Conflict of Interest

The authors declare no conflict of interest.

**Keywords:** methane · dry reforming · heterogeneous catalysis · supported catalysts · nickel · cobalt · alumina

[1] P. Mäki-Arvela, N. Kumar, D. Kubička, A. Nasir, T. Heikkilä, V. P. Lehto, R. P. Sjöholm, T. Salmi, D. Yu. Murzin, *J. Mol. Catal. A* **2015**, *240*, 72–81.
[2] I. Hachemi, N. Kumar, P. Mäki-Arvela, J. Roine, M. Peurla, J. Hemming, J. Salonen, D. Yu. Murzin, *J. Catal.* **2017**, *347*, 205–221.
[3] C. Lindfors, P. Mäki-Arvela, P. Paturi, A. Aho, K. Eränen, J. Hemming, M. Peurla, D. Kubička, I. L. Simakova, D. Yu. Murzin, *ACS Sustainable Chem. Eng.*. **2019**, *7*, 14545–14560.
[4] S. Sengupta, K. Ray, G. Deo, *Int. J. Hydrogen Energy* **2014**, *39*, 11462–11472.
[5] J. Ni, L. Chen, J. Lin, S. Kawi, *Nano Energy* **2012**, *1*, 674–686.
[6] K. Cao, M. Gong, J. Yang, J. Cai, S. Chu, Z. Chen, B. Shan, R. Chen, *J. Catal.* **2019**, *373*, 351–360.
[7] A. Ali, M. M. Khader, M. J. Almarri, A. G. Abdelmoneim, *Catal. Today* **2019**, *343*, 26–37.
[8] J. Cai, J. Zhang, K. Cao, M. Gong, Y. Lang, X. Liu, B. Shan, R. Chen, *ACS Appl. Nano Mat.* **2018**, *1*, 522–530.
[9] K. Cao, L. Shi, M. Gong, J. Cai, X. Liu, S. Chu, Y. Lang, B. Shan, R. Chen, *Small* **2017**, *13*, 1700648.
[10] M. G. Jeong, I. H. Kim, S. W. Han, D. H. Kim, Y. D. Kim, *J. Mol. Catal. A* **2016**, *414*, 87–93.
[11] H. Ay, D. Üner, *Appl. Catal. B.* **2015**, *179*, 128–138.
[12] S. Das, M. Sengupta, A. Bag, M. Shah, A. Bordoloi, *Nanoscale* **2018**, *10*, 6409–6425.
[13] H. Wu, H. Liu, W. Yang, D. He, *Catal. Sci. Technol.* **2016**, *6*, 5631–5646.
[14] T. J. Siang, S. Singh, O. Omoregbe, L. G. Bach, N. H. H. Phuc, D. V. N. Vo, *J. Energy Inst.* **2018**, *91*, 683–694.
[15] Y. F. Adans, A. D. Ballarini, A. R. Martins, R. E. Coelho, L. S. Carvalho, *Catal. Lett.* **2017**, *147*, 2057–2066.
[16] D. San José-Alonso, M. J. Illán-Gómez, M. C. Román-Martínez, *Int. J. Hydrogen Energy* **2013**, *38*, 2230–2239.
[17] Z. Wu, B. Yang, S. Miao, W. Liu, J. Xie, S. Lee, M. J. Pellin, D. J. Xiao, D. Su, D. Ma, *ACS Catal.* **2019**, *9*, 2693–2700.
[18] T. A. Le, T. W. Kim, S. H. Lee, E. D. Park, *Korean J. Chem. Eng.* **2017**, *34*, 3085–3091.

[19] E. Husson, Y. Repelin, *Eur. J. Solid State Inorg. Chem.* **1996**, *33*, 1223–1231.
[20] F. R. Feret, D. Roy, C. Boulanger, *Spectrochim. Acta Part B* **2000**, *55*, 1051–1061.
[21] P. Trucano, R. Chen, *Nature, London, UK* **1975**, *258*, 136–137.
[22] J. P. Picard, G. Baud, J. P. Besse, R. Chevalier, *J. Less-Common Met.* **1980**, *75*, 99–104.
[23] S. Greenwald, *Acta Crystallogr.* **1953**, *6*, 396–398.
[24] S. Sasaki, K. Fujino, Y. Takeuchi, *Proc. Japan Acad.* **1979**, *55*, 43–48.
[25] H. Nakatsugawa, H. M. Jeong, R. H. Kim, N. Gomi, *Jpn. J. Appl. Phys. Part 1* **2007**, *46*, 3004–3012.
[26] H. S. C. O' Neill, W. A. Dollase, C. R. Ross, *Phys. Chem. Miner.* **1991**, *18*, 302–319.
[27] O. Knop, K. I. G. Reid, R. Sutarno, Y. Nakagawa, *Can. J. Chem.* **1968**, *467*, 3463–3476.
[28] P. Garcia Casado, I. Rasines, *J. Solid State Chem.* **1984**, *52*, 187–193.
[29] K. Takanabe, K. Nagaoka, K. Nariai, K. Aika, *J. Catal.* **2005**, *232*, 268–275.
[30] J. Bandyopadhyay, K. P. Gupta, *Cryogenics* **1977**, *17*, 345–347.
[31] E. A. Owen, D. Madoc Jones, *Proc. Phys. Soc. London* **1954**, *67*, 456–466.
[32] A. S. Al-Fatesh, J. K. Abu-Dahrieh, H. Atia, U. Armbruster, A. A. Ibrahim, W. U. Khan, A. E. Abasaeed, A. H. Fakeeha, *Int. J. Hydrogen Energy* **2019**, *44*, 21546–21558.
[33] S. Andonova, C. N. De Ávila, K. Arishtirova, J. M. C. Bueno, S. Damyanova, *Appl. Catal. B* **2011**, *105*, 346–360.
[34] K. V. Chary, P. V. R. Rao, V. V. Rao, *Catal. Commun.* **2008**, *9*, 886–893.
[35] D. Yu. Murzin, *Engineering Catalysis*, De Gruyter, Berlin/Boston, **2013**.
[36] D. San-José-Alonso, J. Juan-Juan, M. J. Illán-Gómez, M. C. Román-Martínez, *Appl. Catal. A* **2009**, *371*, 54–59.
[37] S. Bang, E. Hong, S. W. Baek, C. H. Shin, *Catal. Today* **2018**, *303*, 100–105.
[38] J.-H. Kim, D. Suh, T.-J. Park, K.-L. Kim, *Appl. Catal. A* **2000**, *197*, 191–200.
[39] Z. Xu, Y. Li, J. Zhang, L. Chang, R. Zhou, Z. Duan, *Appl. Catal. A* **2001**, *210*, 45–53.
[40] H. Liu, D. Wierzbicki, R. Debek, M. Motak, T. Grzybek, P. Da Costa, M. E. Gálvez, *Fuel* **2016**, *182*, 8–16.
[41] K. Krishnamoorthy, M. S. P. Sudhakaran, P. Pazhamalai, V. K. Mariappan, Y. S. Mok, S. J. Kim, *J. Mater. Chem. A.* **2019**, *7*, 18950–18958.
[42] M. Ding, Y. Yang, Y. Li, T. Wang, L. Ma, C. Wu, *Appl. Energy* **2013**, *112*, 1241–1246.

Submitted: March 30, 2021
Accepted: March 30, 2021